Small Structures

www.small-structures.com

RESEARCH ARTICLE OPEN ACCESS

Electric Field Enhancements and Hot Spots in Amorphous Carbon Materials

Pablo Grobas Illobre[1] | Giorgio Conter[2] | Luca Bonatti[1] | Tommaso Giovannini[3] | Alessandro Fortunelli[2] |
Chiara Cappelli[1]

[1]Classe di Scienze, Scuola Normale Superiore, Pisa, Italy | [2]Institute of Chemistry of OrganoMetallic Compounds, Consiglio Nazionale delle Ricerche (CNR-ICCOM), Pisa, Italy | [3]Department of Physics, University of Rome Tor Vergata, Rome, Italy

Correspondence: Tommaso Giovannini (tommaso.giovannini@uniroma2.it) | Alessandro Fortunelli (alessandro.fortunelli@cnr.it) | Chiara Cappelli (chiara.cappelli@sns.it)

Received: 13 October 2025 | **Revised:** 9 December 2025 | **Accepted:** 15 December 2025

Keywords: amorphous carbon | atomistic | field enhancement | hot spots | plasmonics

ABSTRACT

Amorphous carbon (a-C) represents a broad and technologically relevant class of carbonaceous materials whose rich morphological diversity, characterized by nanoporosity and defective networks, endows them with unique electrical, chemical, and optical properties. Despite their potential for light–matter interaction and enhanced-chemistry applications, a microscopic understanding of the optical response of a-C remains elusive, primarily due to the absence of long-range order and the resulting need to model systems containing hundreds of thousands of atoms. In this work, we combine atomistic models generated through the dynamic reactive massaging of the potential energy surface (DynReaxMas) approach with a recently developed, fully classical yet atomistic method for calculating their optical response, named frequency-dependent fluctuating charges (ωFQ). This methodology enables the simulation of large-scale a-C structures with near–*ab initio* accuracy, unveiling a complex optical behavior characterized by strong and spatially inhomogeneous local field enhancements ("hot spots"). Four distinct types of hot spots are identified, corresponding to unsaturated carbon dangling bonds, confined regions between graphene-like sheets, single carbon chains, and atomistic defects. Our results demonstrate that these localized field enhancements can, in principle, drive selective sensing and photochemical activity in a-C materials, thereby providing a microscopic basis for their design and functionalization in optical and catalytic applications.

1 | Introduction

Amorphous carbon (a-C) is a commonly employed label term for a broad class of carbonaceous materials which, at variance with diamond, graphite, graphene [1–3], nanotubes [4, 5], cyclocarbons [6–8], and other more regular allotropes [9], do not present long-range structural order [10, 11]. Due to the greater freedom associated with the lack of repetitive units, these materials can exhibit unique and diverse morphological features such as nanoporosity (possibly multimodal), curved traits, tunnels, rough or smooth surfaces, and any combination thereof. This structural freedom, combined with the rich chemistry of carbon, endows them with remarkable electrical, optical, chemical, and mechanical properties, which, apart from an intrinsic scientific interest, make them very attractive and widely exploited in applications, from photoelectrocatalysis to smart materials, to energy storage, to sensing [11–15]. Some of these potential applications are inherently linked to their optical response. In particular, their disordered morphology, characterized by subnanometric gaps, irregular curvatures, and atomistic defects, provides a versatile platform for generating strong and spatially inhomogeneous local field enhancements. Such features make these materials especially appealing for light–matter interaction phenomena relevant to enhanced chemistry, from spectroscopic signals [16–18] to photocatalytic processes, such as CO_2 reduction [19–23], where localized hot spots can selectively modify the electronic structure of adsorbed molecular species.

Deploying this appealing and ambitious strategy presents two major challenges. First, knowledge of the atomistic structure of a-C materials is a prerequisite, a task achieving which is far from trivial for phases with an intrinsic multiscale amorphous character, as witnessed by the many different approaches proposed in the literature to generate their atomistic configurations, from Monte Carlo [24–26] to reactive molecular dynamics [27–32] to the reactive packing of molecular building blocks [33–37]. Indeed, the lack of long-range order combined with a rugged potential energy landscape [38], exhibiting a multitude of local minima separated by high energy barriers associated with breaking/reforming strong covalent bonds, makes it very difficult to first produce and then identify typical configurations.

Second, again due to the lack of long-range order, the size of the systems that need to be dealt with to achieve realistic and accurate structural models is very large, counting at least several thousands atoms (more precisely: from several tens of thousands to millions of atoms) [27, 32]. Accurately describing the optical response of systems of such size is particularly challenging. In fact, conventional methods for the prediction of excited-state and optical properties, such as time-dependent density functional theory (TDDFT), can be applied only to systems containing a few hundred atoms [39]. Even when resorting to semi-empirical extensions, such as time-dependent density functional tight-binding (TDDFTB) [40], the accessible system size can be extended to a few thousand atoms, which is far from the typical size of a-C.

Here, we propose a practical path to realize the strategy outlined above. To address the first challenge, we use atomistic models generated via the dynamic reactive massaging of the potential energy surface (DynReaxMas) approach [27, 32]. DynReaxMas has been designed to run within affordable time scales at realistic simulation temperatures (1500–2000 K), thus managing to correctly capture the interplay of activated versus diffusional processes and the resulting phase morphology in the simulation of the growth. This entails that the resulting DynReaxMas structures can reproduce simultaneously both medium-length-scale and microscopic atomistic features of a-C phases (indeed, a proper account of medium-range structural features is necessary to get correct atomistic structures) in excellent agreement with experimental high-resolution transmission electron microscopy imaging, as well as pair distribution profiles of interatomic distances and several other descriptors fully in tune with experimental phases [27, 32]. Also, collateral properties such as the mechanical behavior are predicted to be in good agreement with experimental data [41].

To address this second challenge and accurately predict the optical response of such large systems, we employ a recently developed fully classical yet atomistic approach, named frequency-dependent fluctuating charges (ωFQ) method [42–45]. This framework models the linear optical response of carbon-based materials by assuming a Drude-like conduction mechanism modulated by quantum tunneling effects [43]. Owing to its classical formulation and favorable computational scaling, ωFQ can be applied to systems comprising hundreds of thousands to millions of atoms, such as a-C, while retaining near–*ab initio* accuracy. In fact, ωFQ provides an accuracy comparable to that of *ab initio* methods for graphene-based nanostructures of various sizes and shapes [43], and it also captures the optical response of graphene nanogaps [46] and defected polycrystalline graphene [47].

We find that a-C materials exhibit an interesting optical response, exhibiting regions of strong electric field enhancement corresponding to "hot spots" of four types depending on the nature of the a-C: (1) unsaturated carbon dangling bonds, (2) confined regions between parallel graphene-like sheets, (3) single carbon chains, and (4) atomistic defects. Our findings demonstrate that selective sensing of molecular species via hot spot electric field enhancement in a-C materials is indeed possible and opens the path to its fundamental understanding and eventual exploitation for technological and chemical applications.

The article is organized as follows. Section 2 describes our methodological tools. Section 3 reports and discusses our results. Section 4 summarizes our findings and conclusions.

2 | Methods

2.1 | DynReaxMas

The DynReaxMas approach combines reactive molecular dynamics with potential energy surface (PES) deformation techniques to achieve highly realistic atomistic configurations while keeping simulated times within very affordable levels (<0.5 ns). The approach is generally applicable and can be implemented using a variety of force fields, here we follow our original work from ref. [27], in which the ReaxFF potential [48] has been employed to describe the PES. This choice is justified by the multiple perks of the ReaxFF. First, there exists an accurate parameterization for carbonaceous materials that includes noncrystalline carbon phases in its training set: the C-2013 forcefield [49]. Second, most ReaxFF parameters have a clear physical interpretation, providing us with more physical ground in selecting the parameters to be worked on during the PES deformation step, which we call a "massage". Third, ReaxFF is widely available for use in many widespread software packages, both open source (such as LAMMPS) and proprietary (SMC, Materials Studio, …), and, thanks to the KOKKOS library [50], can run on GPUs with a >tenfold acceleration with respect to CPU-only machines for systems of the size investigated here. Fourth, ReaxFF performs well in terms of accuracy and comparison with experiment with competitor force fields [51]. Finally, the inclusion of other elements is easier with the ReaxFF than with other similarly accurate potentials (for instance, EDIP [52]), thus making heteroatom inclusion possible.

More in detail, the DynReaxMas protocol works as follows. The starting point is a random configuration of carbon atoms in a cubic simulation box with a proper atom number to cell size ratio to target the desired final density of the model. Then, a short 50 ps molecular dynamics run is performed on the massaged PES that is obtained by halving one of the 15 ReaxFF parameters that are related to interconversion barriers, which include bond breaking, but also rotations and torsions. The procedure is then repeated seven more times by massaging different ReaxFF parameters, to yield a total of eight iterations. Finally, a global optimization step is performed to reduce the amount of high-energy defects. In principle, there exists a very large number of combinations of massage parameters, and the flexibility of the approach relies on the fact that not all massages yield models with the same features. In this work we take the structures from ref. [27] by choosing the ones with the most diverse descriptors. For the sake of simplicity, we streamline the original massage notation, from MMn/MMm into Mnm, so, the structure refered to as MM1/MM8 in [27], will become M18 in this work, and analogously for the other cases. Further information on the rationale behind the DynReaxMas strategy given in Section S1 of the Supporting Information.

Besides the PES deformation, the other relevant parameter of MD for our application is the temperature. The DynReaxMas works at typically lower temperatures than other reactive MD methods, ranging between 1500 and 2500 K. Temperature has a major effect on the morphology of the structures. As expected, higher temperatures lead to a higher degree of graphitization, with more regular sheets and a higher ratio of 6-member rings to 5- or 7-member ones. Most importantly, by playing with the nature of the massages and the temperature, we can generate structures with a different degree of defectivity (e.g. unsaturated bonds), or regularity of the sheets (see also Section S1.2 of the Supporting Information). This allows us to better understand the effect that these structural features have on field enhancement in carbonaceous amorphous phases.

Additionally, in order to expand our database to include more regular yet morphologically complex structures, we also recently introduced into the DynReaxMas protocol a post-processing step [32], i.e., a high temperature treatment, that we call curing. This consists of running a 5 ns MD at 2500 K on the structure resulting from the massaging stage. This high-temperature post-processing does not destroy the overall morphology of the DynReaxMas as-produced phase, but leads to a local rearrangement of the bond structure, without oversimplifying the mesoscale, as it happens instead in other computational protocols when structures are generated at very high temperatures in the growth phase. Moreover, this curing step also has the benefit of closely mimicking the high-temperature post-processing treatments that are typically realized at the experimental level, precisely to reduce the defectivity of the as-prepared experimental phases.

Specifically, in this paper, we explore the optical response of five structures. Since the initial guess is the same for all of them, we can unambiguously refer to them through the massage sequence, the temperature, and whether they are cured or not. Under this convention, we have the M18–2000 uncured and cured, the M34–2000 uncured and cured, and the M18–2500 cured structures.

We focus on a-C phases at a mass density of $\rho = 0.50$ g/cm^3. This is the density most commonly used in sensing and catalytic applications as it allows the system to exhibit nanopores of reasonable size (between 1 and 4 nm), which then have good transport properties combined with good graphiticity and thus good conducting properties [15] depending on the growth temperature and post-processing treatment. We select DynReaxMas structures generated via two different sets of massages: M18 and M34, which can be taken as representative of a more uniform (M18) versus a bimodal (M34) distribution of pore sizes, see Figure 3 of ref. [27]. Additionally, we compare as-grown DynReaxMas structures (hereafter named "uncured") with structures subjected to the post-processing "curing" treatment as described in Section 2. The curing protocol significantly decreases the number of unsaturated carbon atoms with dangling bonds, and the number of fivefold rings by inducing their migration to the edges of graphitic sheets, improving the smoothness of the graphene-like planes, see ref. [32] for a discussion, Section S1 of the Supporting Information for more quantitative analysis, and more details on the curing protocol. Figure S1 of the Supporting Information shows schematic depictions of the phases here considered.

All carbon models were generated according to the DynReaxMas protocol using LAMMPS with 3D PBC. The simulation cells contain 25,056 carbon atoms with an initial periodic cell size of $100 \times 100 \times 100$ Å^3 for $\rho = 0.50$ g/cm^3. The Cartesian coordinates of the structures here employed can be found in the Supporting Information of ref. [32].

2.2 | Frequency-Dependent Fluctuating Charges (ωFQ)

ωFQ is a fully atomistic classical approach designed to investigate the optical response of plasmonic metal nanoparticles [18, 42, 44, 45, 53–58] and carbon-based nanomaterials [43, 46, 47, 59]. In ωFQ, each atom is assigned a complex Gaussian charge distribution that fluctuates under the action of an external monochromatic field oscillating at frequency ω. The charge exchange between the atoms follows the Drude model of conduction, integrated by a phenomenological treatment of quantum tunneling, allowing an accurate description of both local and nonlocal contributions to the optical response [42, 44].

For a system composed of N_{atoms} atoms, in ωFQ the time evolution of the atomic charges is written as [42]:

$$\frac{\mathrm{d}q_i}{\mathrm{d}t} = \sum_{j}^{N_{\text{atoms}}} \mathcal{A}_i \left(n_j \langle \mathbf{p} \rangle \cdot \hat{l}_{ji} - n_i \langle \mathbf{p} \rangle \cdot \hat{l}_{ij} \right) \tag{1}$$

where $\langle \mathbf{p} \rangle$ denotes the average momentum exchanged along the trajectories linking atoms i and j, $\hat{l}_{ij}$ is the unit vector connecting them, and n represents the electronic density. The term $\mathcal{A}_i$ specifies the flux area through which charge exchange takes place.

In the frequency domain, ωFQ charges are computed by solving [42, 43, 59]:

$$-i\omega q_i = \frac{2\tau v_{\mathrm{F}}}{1 - i\omega\tau} \sqrt{\frac{n}{\pi}} \sum_{j=1}^{N_{\text{atoms}}} \left[1 - f(l_{ij})\right] \cdot \frac{\mathcal{A}_i}{l_{ij}} \cdot \left(\phi_j^{el} - \phi_i^{el}\right) \tag{2}$$

where τ is the scattering time, v_{F} is the Fermi velocity (which for carbon-based materials is fixed to 10^6 m/s). l_{ij} is the atom–atom distance, and ϕ_i^{el} is the electrochemical potential acting on atom i, accounting for the interaction with the external field and the other charges. By following graphene electronic structure [2], in carbon-based materials, the Fermi energy, which is defined as $E_F = \hbar v_{\mathrm{F}} \sqrt{\pi \cdot n}$, can be modulated to modify the electron density. The effective mass in this kind of nanostructures is finally defined as $m^* = \sqrt{\pi \cdot n}/v_{\mathrm{F}}$ [2]. $f(l_{ij})$ is a Fermi-like function which mimics quantum tunneling, which is crucial for correctly describing the optical properties of subnanometer gaps [42, 44, 60–62], and atomistic defects [46, 47, 58], as in a-C nanostructures. It is defined as:

$$f(l_{ij}) = \frac{1}{1 + \exp\left[-d\left(\frac{l_{ij}}{s \cdot l_{ij}^0} - 1\right)\right]} \tag{3}$$

where l_{ij}^0 is the nearest-neighbor atomic distance, and d and s determine the charge–transfer profile. All parameters used in the ωFQ calculations, as well as the dependence of the results on the chosen τ, are presented in Section S2 of the Supporting Information.

Equation (2) is solved for each input frequency. The resulting charges describe a discretized induced density, from which the total induced complex dipole moment and the polarizability tensor (α) can be computed. From the diagonal polarizability imaginary components ($\text{Im}[\alpha_{kk}]$), the absorption cross-section σ^{abs} can be evaluated as:

$$\sigma_k^{\text{abs}}(\omega) = \tfrac{4\pi\omega}{c}\,\text{Im}[\alpha_{kk}(\omega)] \qquad k \in \{x, y, z\} \tag{4}$$

$$\sigma_{\text{iso}}^{\text{abs}}(\omega) = \tfrac{1}{3}\sum_k \sigma_k^{\text{abs}}(\omega) \tag{5}$$

where Equations (4) and (5) represent the absorption cross-section along the k direction, and the isotropic average, respectively. All ωFQ calculations are performed by using plasmonX [63].

In addition, the electric field induced by the charges at a spatial point $\mathbf{r}_p$ can be computed as [44]:

$$\mathbf{E}_X(\mathbf{r}_p) = -\sum_{i=1}^{N_{\text{atoms}}} q_i^X \left[\frac{\mathbf{r}_{ip}}{|\mathbf{r}_{ip}|^3}\left(\text{erf}\left(\frac{|\mathbf{r}_{ip}|}{R_{q_i}}\right) - \frac{2|\mathbf{r}_{ip}|}{\sqrt{\pi}R_{q_i}}\exp\left(-\frac{|\mathbf{r}_{ip}|^2}{R_{q_i}^2}\right)\right)\right] \tag{6}$$

where R_{q_i} is the width of the Gaussian charge distribution associated with the atom i, $\mathbf{r}_{ip}$ is the vector connecting the atom i and the point p, and X indicates whether the real (Re) or imaginary (Im) component of the charge is considered.

From the calculation of the induced electric field in Equation (6), the field enhancement can be calculated at a specific point. This is a fundamental quantity in optical simulations, as it is directly related (through its second and fourth powers) to the enhancements that are measured in surface-enhanced (SE) spectroscopies, such as SE infrared absorption [64–66] and surface-enhanced Raman scattering (SERS) [16, 18, 57, 67–69]. By considering an incoming external field intensity $\mathbf{E}_0$, the field enhancement can be defined as:

$$\frac{|\mathbf{E}(\mathbf{r}_p)|}{|\mathbf{E}_0|} = \frac{\sqrt{|\mathbf{E}_{\text{Re}}(\mathbf{r}_j)|^2 + |\mathbf{E}_{\text{Im}}(\mathbf{r}_j)|^2}}{|\mathbf{E}_0|} \tag{7}$$

3 | Results and Discussion

We begin our discussion by examining the absorption cross sections of the a-C M18–2000 and M34–2000 phases, in both their uncured and cured forms. In this way, a sufficiently large dataset is studied, which allows us to draw meaningful conclusions about the structure–properties relationship. The considered systems are generated by replicating the unit cell 27 times (see Figure 1) along each direction. This procedure ensures that hot spots and their periodic images are spatially separated, effectively removing artificial boundary effects. The resulting M18–2000 and M34–2000 superstructures are composed of 676 512 atoms. The simulation of the optical response of such large structures at full atomistic detail is prohibitive for nearly all atomistic theoretical methods, but ωFQ. In the present work, we take advantage of the favorable scaling of the ωFQ method, which makes it possible to investigate such extended systems with a level of accuracy that is comparable to that of fully *ab initio* methodologies [42, 44, 45].

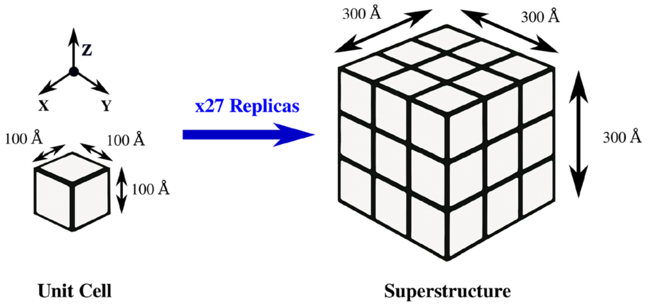

FIGURE 1 | Graphical representation of the simulated unit cell and the a-C superstructure.

ωFQ absorption spectra, computed along the X, Y, and Z directions and normalized with respect to the total number of atoms in the system, are reported in Figure 2, together with their isotropic average. The optical response of all systems is characterized by a main peak at the plasmon resonance frequency (PRF). For the M18–2000 superstructures (Figure 2a,b), the PRF remains essentially unchanged, at ≈0.36 eV, for both the cured and uncured forms. In both cases, the optical response does not exhibit substantial variations as a function of the incident polarization, with all absorption spectra closely following the isotropic average. This behavior is particularly evident for the cured form (Figure 2b). However, the two nanostructures differ significantly in the relative absorption intensities along the three directions, with the X and Z components inverting their relative strength upon curing. Notably, our results are consistent with experimental observations on related nanoporous carbon systems, where mid-infrared plasmons are found at comparable energies for Fermi levels similar to those used in our simulations [70].

In contrast, the M34–2000 superstructures (Figure 2c,d) preserve the same ordering of absorption intensities in both the cured and uncured forms, with the PRF again placed at around 0.36 eV. In this case, the curing process induces a noticeable broadening of the absorption band (Figure 2d). To further investigate this effect, Figure S3 in the Supporting Information compares the cured M34–2000 structure with the cured M34–2500, both generated from a 50% replication of the unit cell. A further broadening of the band is observed, while the PRF remains fixed at 0.36 eV and the relative order of the peak intensities is unchanged. It is also worth noting that, differently from the M18–2000 case, the M34–2000 structures exhibit a clear anisotropy in both forms. In particular, the X absorption substantially deviates from Y, Z, and from the isotropic average.

The overall optical response appears similar across all the studied systems, in both cured and uncured forms. Nevertheless, subtle differences arise, hinting at underlying distinct structural morphologies. To gain a more comprehensive understanding of this relationship, we analyze the enhancement of the electric field

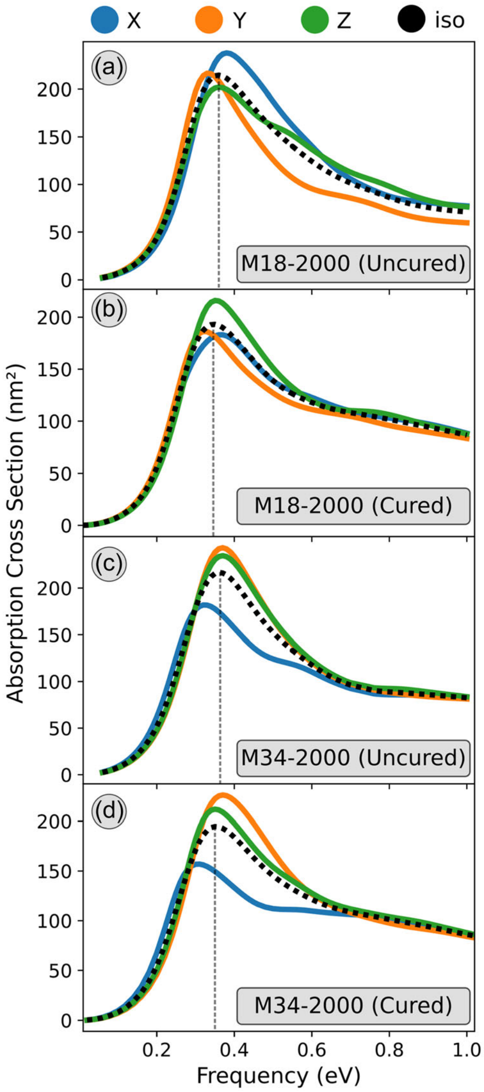

FIGURE 2 | ωFQ absorption cross section of M18−2000 (a,b) and M34−2000 (c-) a-C superstructures, in their uncured (a,c) and cured (b,d) forms. Vertical dashed lines indicate the PRF.

(see Equation (7)) as calculated at the PRF for an incident field polarized along the X, Y, and Z axes.

In Figure 3, we report the electric field enhancements as three-dimensional density maps computed within the unit cell (isovalue = 0.4). This representation highlights the regions where the local field enhancement reaches maximum intensity. By first focusing on the M18−2000 systems (Figure 3, first and second columns), we observe that in the uncured form, the field enhancement appears to be confined to smaller regions, whereas the cured morphology displays more extended domains characterized by strong enhancements for X and Y polarization directions of the applied electric field. In contrast, the M34−2000 systems (Figure 3, third and fourth columns) exhibit only minor differences in field localization between their cured and uncured forms. Nevertheless, the cured morphology shows a tendency toward more localized field enhancements, particularly evident for external field polarizations along the Y and Z directions (see Figure 3b,c). All these trends are a direct consequence of the induced charge density calculated at the corresponding PRFs (see Figure S4 in the Supporting Information).

To gain further insight into this behavior, we analyze the field enhancements on planes orthogonal to the incident polarization (see Figure 3), spanning the unit cell from 0 to 10 nm with constant steps of 1 nm (see Figures S5–S16 in the Supporting Information). For each incident field direction, representative planes of each structure are selected to highlight regions of strong field enhancement and relate them to relevant morphological features (see Figure 3). We immediately state that four diverse hot-spot regions can be recognized, characterizing each structure (vide infra): stacked graphene-like sheets, dangling bonds, single carbon chains, and atomistic defects. Notably, the maximum value shown in the color scale of each plane might not correspond to the global maximum field enhancement reported in Table 1, as the sliced planes do not necessarily intersect the exact spatial location where the maximum enhancement occurs.

A comparison between the cured and uncured M18−2000 structures (Figure 3, first and second columns) reveals that the uncured form develops pronounced hot spots originating from regions where graphene-like sheets are arranged in a stacking configuration (see highlighted red portions). These stacked hot spots are less present in the cured structure, which nonetheless exhibits more localized regions of strong field enhancement, associated with atomistic defects. In contrast, the M34−2000 systems (Figure 3, third and fourth columns) display significant modifications in the topology of the hot spots. As an example, in the case of a Z-polarized incident field (Figure 3c), the uncured structure exhibits a very delocalized enhancement within a single carbon chain, whereas the corresponding cured structure displays a stacking-like topology that is, however, much more localized. We further note that in the M34−2000 cured system, the Y-polarized incident field gives rise to extremely intense and highly localized field enhancements associated with single carbon chains and atomistic defects, reaching values of about 40. Remarkably, such a strong enhancement might, in principle, correspond to a SERS amplification on the order of 10^6 ($|E|^4/|E_0|^4$ [16], which is typical for noble-metal nanostructures but has never been reported in the context of carbon-based nanostructures [71, 72]. We note that such enhancement factors can also be influenced by the adsorption geometry and by the laser frequency, which can resonate with molecular electronic transitions, providing an additional enhancement mechanism. This observation, therefore, highlights a promising potential application of these substrates that could propel further experimental investigations.

To quantify the qualitative differences highlighted in Figure 3, we calculate the effective volume $\mathcal{V}$, which is defined as [73–75]:

$$\mathcal{V} = \int_{\Omega} \frac{|\mathbf{E}(\mathbf{r})|^2}{|\mathbf{E}^{\max}|^2} \mathrm{d}^3\mathbf{r} \tag{8}$$

where $\mathbf{E}^{\max}$ is the maximum of the induced electric field $\mathbf{E}(\mathbf{r})$ in the studied volume Ω (in this case, the unit cell highlighted in Figure 3). The effective volume $\mathcal{V}$ provides a quantification of the localization of the induced electric field [73–75]. The numerical values of $\mathcal{V}$ for the studied systems as a function of the incident field polarization calculated at the PRF are reported in Table 1, together with the computed maximum field enhancement observed in the volume Ω. We remark that the values reported in Table 1 for the maximum $|E|/|E_0|$ and the effective volume are computed over the central unit cell of the a-C superstructure.

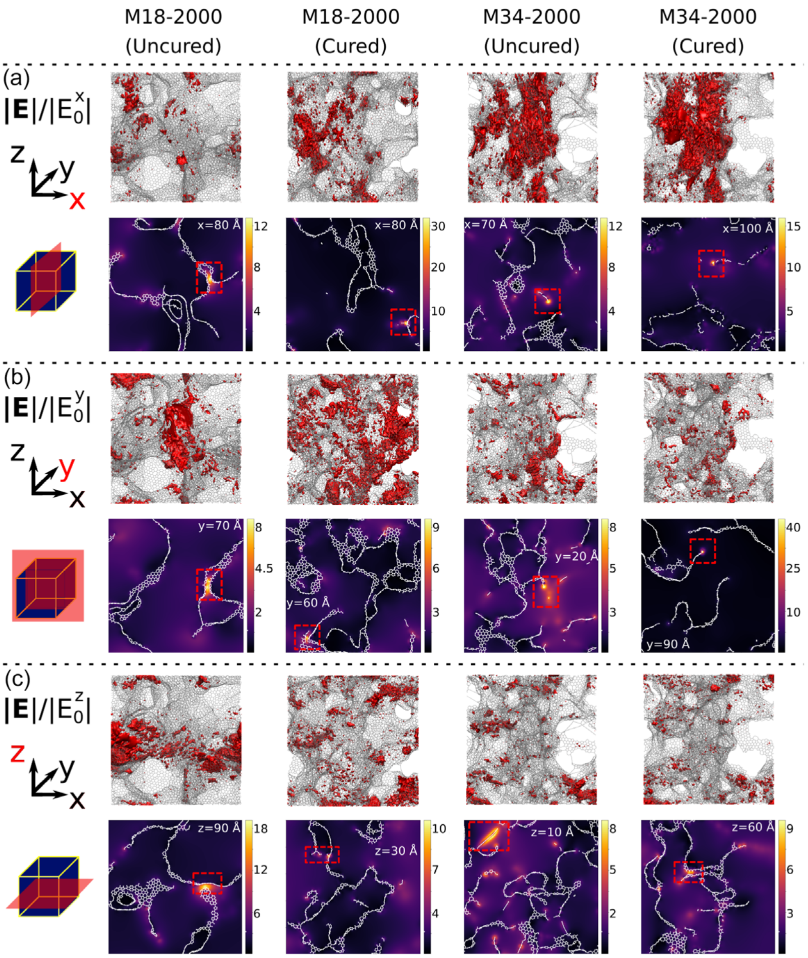

FIGURE 3 | ωFQ electric field enhancements for *X* (a), *Y* (b), and *Z* (c) field polarizations, depicted as 3D density maps (top) and 2D color maps on planes orthogonal to field propagation (see left panel) for M18–2000 and M34–2000 in their uncured and cured forms. The maps are provided within the central unit cell.

TABLE 1 | Effective volume and maximum electric field enhancement $|E|/|E_0|$ for M18–2000 and M34–2000 a-C superstructures in their uncured and cured forms as a function of the field polarization calculated within the central unit cell. Average values are reported as $\langle\cdot\rangle$.

	Effective volume (nm^3)			
	M18–2000		**M34–2000**	
Polarization	**Uncured**	**Cured**	**Uncured**	**Cured**
$\vec{E}_x$	9.16	1.38	1.78	3.33
$\vec{E}_y$	7.22	7.34	13.68	1.88
$\vec{E}_z$	1.78	6.56	10.43	2.51
Average	6.05	5.09	8.63	2.57

	Maximum $\mathbf{|E|/|E_0|}$			
	M18–2000		**M34–2000**	
Polarization	**Uncured**	**Cured**	**Uncured**	**Cured**
$\vec{E}_x$	18.64	49.98	18.11	29.28
$\vec{E}_y$	21.73	20.07	15.41	43.74
$\vec{E}_z$	43.31	19.69	17.01	34.92
$\langle|E|/|E_0|\rangle$	27.89	29.91	16.84	35.98
$\langle|E|/|E_0|\rangle^4$	6.05×10^5	8.00×10^5	8.04×10^4	1.68×10^6

For both the M18–2000 and M34–2000 structures, the effective localization volume is, on average, larger in the uncured forms than in the cured ones. This indicates that the curing process leads to a stronger confinement of the electric field within specific regions. This trend is consistent with the 2D field enhancement maps shown in Figure 3. In fact, we noted above that the uncured structures exhibit more delocalized regions of enhancement, corresponding to the stacked graphene-like microenvironments. The difference between the uncured and cured morphologies is particularly pronounced for M34–2000, where the curing process drastically reduces the effective field volume (from 8.63 to 2.57). It should be noted, however, that this observation is valid on average, while for specific field polarizations, the trend may be reversed (as for Z and X directions for M18–2000 and M34–2000, respectively).

The overall behavior can be rationalized by referring to the 3D field enhancement maps in Figure 3. For example, in Figure 3b, corresponding to Y polarization, the electric field distribution shows that the uncured structure exhibits a more delocalized field compared to the cured one, in agreement with the effective volume values reported in Table 1. For other polarizations, however, this correspondence is not as straightforward, underscoring the importance of the present quantitative analysis. To further explore this aspect, Table S5 in the Supporting Information reports the effective volume and effective area corresponding to the red-highlighted regions in Figure 3. The effective volume is defined within a slab of thickness ±1 Å along the coordinate normal to the plane, whereas the effective area is computed as $\mathcal{A} = \mathcal{V}/h$, where h denotes the slab thickness along the normal direction. In line with the trends discussed above, both the effective volume and the effective area of the marked regions are significantly larger in the uncured structures than in their cured counterparts, for both M18–2000 and M34–2000.

The effective volume $\mathcal{V}$ is directly related to the maximum value of the electric field within the studied volume Ω (see Equation (8)). In Table 1, we also report the maximum field enhancement $|E|/|E_0|$ for the various field polarizations. On average, the electric field enhancement is larger for the cured structures. This behavior is consistent with the stronger field localization observed in these systems. Similarly to what was found for the effective volume, the maximum field enhancement more than doubles for M34–2000 upon curing, while for M18–2000, the increase is around 7%. For the M18–2000 structures, however, the X and Z polarizations display the opposite trend in both $\mathcal{V}$ and the maximum field enhancement after curing. This inversion directly mirrors the change in the relative absorption peak intensities observed in Figure 2a,b. Such a correspondence highlights the inherent connection between the different optical response quantities that can be computed using the ωFQ method and the underlying structural morphology.

To establish a final structure–property connection, Figure 4 provides a graphical representation of the spatial locations corresponding to the maximum field enhancements reported in Table 1. Each panel offers a visual overview of the different hot-spot regions discussed above. In the case of the M18–2000 uncured structure, the maximum enhancement is localized within stacked graphene-like sheets for the X and Y polarizations. Similar regions are also observed for the cured morphology under Y polarization, whereas for the Z polarization in the cured form, the enhancement is mostly localized near dangling bonds.

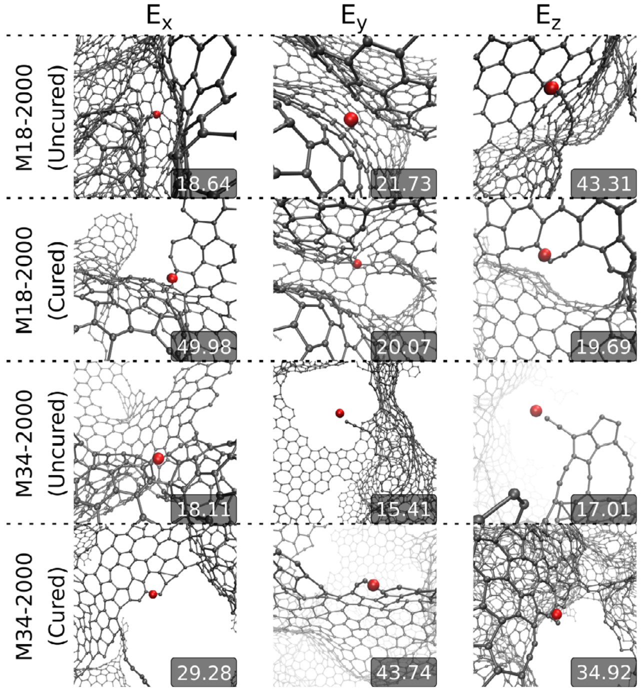

FIGURE 4 | Spatial locations of the maximum field enhancement (red dots) identified for the M18–2000 and M34–2000 structures in their uncured and cured morphologies.

In contrast, for the M34–2000 system in the uncured form, the regions of maximum enhancement correspond to single carbon-chain domains for the Y and Z polarizations and to dangling bonds for the X polarization. The remaining enhancement regions are mainly associated with atomistic defects. These features are generally present in the cured morphologies (M34–2000, all polarizations; and M18–2000, X polarization), but can also appear in the uncured forms, as observed for the Z polarization in M18–2000. It is worth noting that these defect-related regions correspond to the strongest local field enhancements, which can reach values close to 50 (M18–2000, X polarization). This behavior is expected, since subnanometer gaps [60] with atomistic features are formed, giving rise to unique plasmonic characteristics analogous to those reported for atomically defective metallic nanostructures, such as picocavities [58, 62, 74, 75].

All of our findings can be rationalized by considering that the curing process relaxes the atomic network, resulting in more localized atomic defects. In contrast, the uncured structures tend to preserve stacked domains and dangling atoms, which, on average, increase the effective field volume and, correspondingly, reduce the maximum field enhancement.

A final note regards the generality of the present results with respect to a-C phases, e.g. at mass density different from $\rho = 0.50$ g/cm^3. Indeed, in our previous work we have investigated phases at both higher (1.15 g/cm^3) and lower (0.16 g/cm^3) mass density. Now, as discussed in the original references, the phases at higher density are intended to mimic a-C coatings, possess limited graphiticity and a large number of sp^3 carbon atoms. They will thus basically not exhibit stacked graphene planes, nor chains, but they may exhibit defects and unsaturated atoms, that will therefore determine their optical response. The phases at a lower mass density, that we claim are the structural basis of carbon aerogels [41], are instead more diverse, ranging from very sparse carbon networks to 1D-fiber-like clumps interconnected with filaments or strings. Here we expect to encounter a higher percent of chain motifs in the filaments, whereas the fiber-like motifs may exhibit a significant optical response, but of possibly limited use, e.g. in sensing due to the inability of species to be sensed to access the interstacking regions where the resonance will reach its maximum. How to engineer a-C phases to maximize the presence of stacked graphitic planes at a proper distance optimal for sensing represents a question that we are unable to answer at present.

4 | Summary and Conclusions

In this work, we have combined large-scale atomistic models of a-C generated by the DynReaxMas protocol with the ωFQ method to understand the structure–property relationships governing their optical response. The DynReaxMas approach enabled us to construct realistic morphologies with hundreds of thousands of atoms, while ωFQ provided near–*ab initio* accuracy at reasonable computational cost for systems of this size. Across all studied superstructures, the absorption spectra exhibit a dominant plasmon resonance at 0.36 eV, with M18−2000 showing nearly isotropic behavior and M34−2000 exhibiting a pronounced anisotropy. Curing produces distinct spectral signatures, which are also deeply connected with electric field enhancements. Our analysis reveals that curing on average increases field localization and the maximum field enhancement, while reducing the effective localization volume, an effect that is particularly marked for M34−2000. By mapping enhancement distributions in 3D and on polarization-orthogonal planes, we identified four recurring classes of hot spots that rationalize the observed trends: (i) unsaturated dangling bonds, (ii) confined regions between stacked graphene-like sheets, (iii) single carbon chains, and (iv) atomistic defects. The most intense enhancements (up to 50 in $|E|/|E_0|$) arise in defect-mediated sub-nanometric gaps, quantitatively en par to that encountered in atomically defective metallic nanojunctions. These results demonstrate a direct link between mesoscale morphology (e.g., stacking motifs, chain segments) and the direction-dependent optical response, thereby providing a microscopic basis for engineering hot-spot topology and strength in a-C.

Our findings establish a practical route to design a-C substrates for enhanced-chemistry applications (e.g., surface-enhanced spectroscopies and photocatalysis): the DynReaxMas + ωFQ workflow connects synthesis-controllable parameters (massage sequence, growth/curing temperature) to the hot-spot profile and field metrics (PRF position, enhancement maxima, effective volumes). Future work will extend this framework to heteroatom-doped and functionalized a-C, explore excitation-wavelength and environment (dielectric) dependencies, and pursue experimental validation [76, 77] of predicted hot-spot classes and enhancement factors. This integrated approach opens the way for rational tailoring of a-C for selective sensing and light-driven chemical transformations.

Author Contributions

Giorgio Conter and **Alessandro Fortunelli** performed DynReaxMas calculations. **Pablo Grobas Illobre**, **Luca Bonatti**, and **Tommaso Giovannini** performed ωFQ calculations. All the authors analyzed and discussed the results. **Tommaso Giovannini**, **Alessandro Fortunelli**, and **Chiara Cappelli** supervised the work. All authors contributed to the writing of the manuscript.

Acknowledgments

This project has originated and has been developed within the COST Action CA21101 “Confined molecular systems: from a new generation of materials to the stars” (COSY) supported by COST (European Cooperation in Science and Technology). We gratefully acknowledge the Center for High-Performance Computing (CHPC) at SNS for providing the computational infrastructure. CC and PGI acknowledge funding from MUR-FARE Ricerca in Italia: Framework per l’attrazione ed il rafforzamento delle eccellenze per la Ricerca in Italia - III edizione. Prot. R20YTA2BKZ. AF and GC are grateful to the Cineca Supercomputing Center (Italy) for providing computational resources, and acknowledge financial support under the National Recovery and Resilience Plan (PNRR), Mission 4, Component 2, Investment 1.1, by the Italian Ministry of University and Research (MUR), funded by the European Union – NextGenerationEU – Project COCAP, and from ICSC, the Italian Centro Nazionale di Ricerca in High Performance Computing, Big Data and Quantum Computing, funded by the European Union (Next Generation EU, grant number CN00000013).

Open access publishing facilitated by Scuola Normale Superiore, as part of the Wiley - CRUI-CARE agreement.

Conflicts of Interest

The authors declare no conflicts of interest.

Data Availability Statement

The data that support the findings of this study are available from the corresponding author upon reasonable request.

References

1. A. K. Geim and K. S. Novoselov, “The Rise of Graphene,” *Nature Materials* 6, no. 3 (2007): 183–191.

2. A. H. C. Neto, F. Guinea, N. M. R. Peres, K. S. Novoselov, and A. K. Geim, “The Electronic Properties of Graphene,” *Reviews of Modern Physics* 81, no. 1 (2009): 109.

3. A. N. Grigorenko, M. Polini, and K. S. Novoselov, “Graphene Plasmonics,” *Nature Photonics* 6, no. 11 (2012): 749–758.

4. M. S. Dresselhaus, G. Dresselhaus, P. C. Eklund, A. M. Rao, “Carbon Nanotubes,” in *The Physics of Fullerene-Based and Fullerene-Related Materials* (Springer, 2000), 331–379.

5. D. Tasis, N. Tagmatarchis, A. Bianco, and M. Prato, “Chemistry of Carbon Nanotubes,” *Chemical Reviews* 106, no. 3 (2006): 1105–1136.

6. K. Kaiser, L. M. Scriven, F. Schulz, P. Gawel, L. Gross, and H. L. Anderson, “An sp-Hybridized Molecular Carbon Allotrope, Cyclo [18] Carbon,” *Science* 365, no. 6459 (2019): 1299–1301.

7. F. Albrecht, I. Rončević, Y. Gao, et al., “The Odd-Number Cyclo [13] Carbon and its Dimer, Cyclo [26] Carbon,” *Science* 384, no. 6696 (2024): 677–682.

8. L. Sun, W. Zheng, W. Gao, F. Kang, M. Zhao, W. Xu, “On-Surface Synthesis of Aromatic Cyclo [10] Carbon and Cyclo [14] Carbon,” *Nature* 623, no. 7989 (2023): 972–976.

9. A. Hirsch, “The Era of Carbon Allotropes,” *Nature Materials* 9, no. 11 (2010): 868–871.

10. Y. Liu, A. Madanchi, A. S. Anker, L. Simine, and V. L. Deringer, “The Amorphous State as a Frontier in Computational Materials Design,” *Nature Reviews Materials* 10, no. 3 (2025): 228–241.

11. J. Robertson, “Amorphous Carbon,” *Advances in Physics* 35, no. 4 (1986): 317–374.

12. D. M. Anjo, M. Kahr, M. M. Khodabakhsh, S. Nowinski, and M. Wanger, “Electrochemical Activation of Carbon Electrodes in base: Minimization of Dopamine Adsorption and Electrode Capacitance,” *Analytical Chemistry* 61, no. 23 (1989): 2603–2608.

13. P. Qi, S. Chen, J. Chen, J. Zheng, X. Zheng, and Y. Yuan, “Catalysis and Reactivation of Ordered Mesoporous Carbon-Supported Gold Nanoparticles for the Base-Free Oxidation of Glucose to Gluconic Acid,” *ACS Catalysis* 5, no. 4 (2015): 2659–2670.

14. Y. Zhao, X. Min, Z. Ding, et al., “Metal Based Nanocatalysts via a Universal Design on Cellular Structure,” *Advancement of Science* 7, no. 3 (2020): 1902051.

15. H.-Y. Lee, T. H. Yu, C.-H. Shin, et al., “Low Temperature Synthesis of New Highly Graphitized N-Doped Carbon for Pt Fuel Cell Supports, Satisfying DOE 2025 Durability Standards for both Catalyst and Support,” *Applied Catalysis B: Environmental* 323 (2023): 122179.

16. J. Langer, D. J. de Aberasturi, J. Aizpurua, et al., “Present and Future of Surface-Enhanced Raman Scattering,” *ACS Nano* 14, no. 1 (2020): 28–117.

17. L. Jensen, C. M. Aikens, and G. C. Schatz, “Electronic Structure Methods for Studying Surface-Enhanced Raman Scattering,” *Chemical Society Reviews* 37, no. 5 (2008): 1061–1073.

18. P. Lafiosca, L. Nicoli, L. Bonatti, T. Giovannini, S. Corni, and C. Cappelli, “QM/Classical Modeling of Surface Enhanced Raman Scattering Based on Atomistic Electromagnetic Models,” *Journal of Chemical Theory and Computation* 19, no. 12 (2023): 3616–3633.

19. E. Cortés, L. V. Besteiro, A. Alabastri, et al., “Challenges in Plasmonic Catalysis,” *ACS Nano* 14, no. 12 (2020): 16202–16219.

20. P. H. C. Camargo, “Emiliano Cortés,” in *Plasmonic Catalysis: From Fundamentals to Applications* (John Wiley & Sons, 2021).

21. P. Ganji, R. K. Chowdari, and B. Likozar, “Photocatalytic Reduction of Carbon Dioxide to Methanol: Carbonaceous Materials, Kinetics, Industrial Feasibility, and Future Directions,” *Energy & Fuels* 37, no. 11 (2023): 7577–7602.

22. N. K. Mohammadi and S. Fatemi, “Efficient Photo-catalytic CO_2 Conversion to CO and CH_4 by a rGO-Bridged g-C_3N_4/MoS_2 Indirect Z-Scheme Heterojunction,” *Industrial & Engineering Chemistry Research* 64, no. 21 (2025): 10399–10413.

23. K. M. Kamal, R. Narayan, and N. Chandran et al., “Synergistic Enhancement of Photocatalytic CO_2 Reduction by Plasmonic Au Nanoparticles on TiO_2 Decorated N-Graphene Heterostructure Catalyst for High Selectivity Methane Production,” *Applied Catalysis B: Environmental* 307 (2022): 121181.

24. J. Pikunic, C. Clinard, N. Cohaut, et al., “Structural Modeling of Porous Carbons: Constrained Reverse Monte Carlo Method,” *Langmuir* 19, no. 20 (2003): 8565–8582.

25. C. Bousige, C. M. Ghimbeu, C. Vix-Guterl, et al., “Realistic Molecular Model of Kerogen’s Nanostructure,” *Nature Materials* 15, no. 5 (2016): 576–582.

26. P. Zetterstrom, S. Urbonaite, F. Lindberg, R. G. Delaplane, J. Leis, and G. Svensson, “Reverse Monte Carlo Studies of Nanoporous Carbon from TiC,” *Journal of Physics: Condensed Matter* 17, no. 23 (2005): 3509.

27. S. Monti, G. Barcaro, W. A. III Goddard, and A. Fortunelli, “Diverse Phases of Carbonaceous Materials from Stochastic Simulations,” *ACS Nano* 15, no. 4 (2021): 6369–6385.

28. L. Atmani, C. Bichara, R. J.-M. Pellenq, et al., “From Cellulose to Kerogen: Molecular Simulation of a Geological Process,” *Chemical Science* 8 (2017): 8325–8335.

29. J. C. Palmer, A. Llobet, S.-H. Yeon, et al., “Modeling the Structural Evolution of Carbide Derived Carbons using Quenched Molecular Dynamics,” *Carbon* 48, no. 4 (2010): 1116–1123.

30. A. Obliger, C. Bousige, B. Coasne, J.-M. Leyssale, “Development of Atomistic Kerogen Models and Their Applications for Gas Adsorption and Diffusion: A Mini-Review,” *Energy & Fuels* 37, no. 3 (2023): 1678–1698.

31. C. de Tomas, I. Suarez-Martinez, F. Vallejos-Burgos, M. J. Lopez, K. Kaneko, and N. A. Marks, “Structural Prediction of Graphitization and Porosity in Carbide-Derived Carbons,” *Carbon* 119 (2017): 1–9.

32. G. Conter, S. Monti, G. Barcaro, W. A. III Goddard, and A. Fortunelli, “Functionalized Amorphous Carbon Materials via Reactive Molecular Dynamics Simulations,” *ACS Applied Materials & Interfaces* 16, no. 36 (2024): 48043–48057.

33. E. Di Biase and L. Sarkisov, “Systematic Development of Predictive Molecular Models of High Surface Area Activated Carbons for Adsorption Applications,” *Carbon* 64 (2013): 262–280.

34. L. Bellucci and V. Tozzini, “Engineering 3D Graphene-Based Materials: State of the Art and Perspectives,” *Molecules* 25, no. 2 (2020): 339.

35. V. L. Deringer and G. Csányi, “Machine Learning based Interatomic Potential for Amorphous Carbon,” *Physical Review B* 95 (2017): 094203.

36. M. A. Caro, G. Csányi, T. Laurila, and V. L. Deringer, “Machine Learning Driven Simulated Deposition of Carbon Films: From Low-Density to Diamond like Amorphous Carbon,” *Physical Review B* 102 (2020): 174201.

37. A. Dernov, M. Kowalik, A. C. T. van Duin, and T. Dumitrică, “Mapping the Structural-Mechanical Landscape of Amorphous Carbon with ReaxFF Molecular Dynamics,” *Journal of Applied Physics* 137, no. 6 (2025): 065107.

38. D. J. Wales, *Energy Landscapes: Applications to Clusters, Biomolecules and Glasses* (Cambridge University Press, 2013).

39. M. Chaudhary and H.-C. Weissker, “Optical Spectra of Silver Clusters and Nanoparticles from 4 to 923 Atoms from the TDDFT+U Method,” *Nature Communications* 15, no. 1 (2024): 9225.

40. G. Seifert and J.-O. Joswig, “Density-Functional Tight Binding—An Approximate Density-Functional Theory Method,” *WIREs Computational Molecular Science* 2, no. 3 (2012): 456–465.

41. G. Conter, K. Xiao, X. Wu, W. A. Goddard, and A. Fortunelli, “Atomistic Mechanisms Underlying Plastic Flow at Ultralow Yield Stress in Ductile Carbon Aerogels,” *Nanoscale* 15, no. 48 (2023): 19709–19716.

42. T. Giovannini, M. Rosa, S. Corni, and C. Cappelli, “A Classical Picture of Subnanometer Junctions: An Atomistic Drude Approach to Nanoplasmonics,” *Nanoscale* 11, no. 13 (2019): 6004–6015.

43. T. Giovannini, L. Bonatti, M. Polini, and C. Cappelli, “Graphene Plasmonics: Fully Atomistic Approach for Realistic Structures,” *The Journal of Physical Chemistry Letters* 11, no. 18 (2020): 7595–7602.

44. T. Giovannini, L. Bonatti, P. Lafiosca, et al., “Do We Really Need Quantum Mechanics to Describe Plasmonic Properties of Metal Nanostructures?,” *ACS Photonics* 9, no. 9 (2022): 3025–3034.

45. L. Nicoli, P. Lafiosca, P. G. Illobre, L. Bonatti, T. Giovannini, and C. Cappelli, “Fully Atomistic Modeling of Plasmonic Bimetallic Nanoparticles: Nanoalloys and Core-Shell Systems,” *Frontiers in Photonics* 4 (2023): 2673–6853.

46. L. Bonatti, L. Nicoli, T. Giovannini, and C. Cappelli, “In Silico Design of Graphene Plasmonic Hot-Spots,” *Nanoscale Advances* 4, no. 10 (2022): 2294–2302.

47. S. Zanotto, L. Bonatti, M. F. Pantano, et al., “Strain-Induced Plasmon Confinement in Polycrystalline Graphene,” *ACS Photonics* 10, no. 2 (2023): 394–400.

48. K. D. Nielson, A. C. T. van Duin, J. Oxgaard, W.-Q. Deng, and W. A. Goddard, “Development of the ReaxFF Reactive Force Field for Describing Transition Metal Catalyzed Reactions, with Application to the Initial Stages of the Catalytic Formation of Carbon Nanotubes,” *The Journal of Physical Chemistry A* 109, no. 3 (2005): 493–499.

49. S. G. Srinivasan, A. C. T. van Duin, and P. Ganesh, “Development of a ReaxFF Potential for Carbon Condensed Phases and Its Application to the Thermal Fragmentation of a Large Fullerene,” *The Journal of Physical Chemistry A* 119, no. 4 (2015): 571–580.

50. C. R. Trott, D. Lebrun-Grandié, D. Arndt, et al., “Kokkos 3: Programming Model Extensions for the Exascale Era,” *IEEE Transactions on Parallel and Distributed Systems* 33, no. 4 (2022): 805–817.

51. C. de Tomas, A. Aghajamali, J. L. Jones, et al., “Transferability in Interatomic Potentials for Carbon,” *Carbon* 155 (2019): 624–634.

52. N. A. Marks, “Generalizing the Environment-Dependent Interaction Potential for Carbon,” *Physical Review B* 63, no. 7 (2000): 035401.

53. L. Bonatti, G. Gil, T. Giovannini, S. Corni, and C. Cappelli, “Plasmonic Resonances of Metal Nanoparticles: Atomistic vs. Continuum Approaches,” *Frontiers in Chemistry* 8 (2020): 340.

54. P. Lafiosca, L. Nicoli, S. Pipolo, S. Corni, T. Giovannini, and C. Cappelli, “Real-Time Formulation of Atomistic Electromagnetic Models for Plasmonics,” *The Journal of Physical Chemistry C* 128 (2024): 17513–17525.

55. P. G. Illobre, P. Lafiosca, T. Guidone, F. Mazza, T. Giovannini, and C. Cappelli, “Multiscale Modeling of Surface Enhanced Fluorescence,” *Nanoscale Advances* 6 (2024): 3410–3425.

56. L. Nicoli, S. Sodomaco, P. Lafiosca, T. Giovannini, and C. Cappelli, “Atomistic Multiscale Modeling of Colloidal Plasmonic Nanoparticles,” *ACS Physical Chemistry Au* 4 (2024): 1199598.

57. P. Grobas Illobre, P. Lafiosca, L. Bonatti, T. Giovannini, and C. Cappelli, “Mixed Atomistic-Implicit Quantum/Classical Approach to Molecular Nanoplasmonics,” *The Journal of Chemical Physics* 162, no. 4 (2025): 044103.

58. T. Giovannini, L. Nicoli, S. Corni, and C. Cappelli, “The Electric Field Morphology of Plasmonic Picocavities,” *Nano Letters* 25, no. 27 (2025): 10802–10808.

59. P. Lafiosca, T. Giovannini, M. Benzi, and C. Cappelli, “Going Beyond the Limits of Classical Atomistic Modeling of Plasmonic Nanostructures,” *The Journal of Physical Chemistry C* 125, no. 43 (2021): 23848–23863.

60. K. J. Savage, M. M. Hawkeye, R. Esteban, A. G. Borisov, J. Aizpurua, and J. J. Baumberg, “Revealing the Quantum Regime in Tunnelling Plasmonics,” *Nature* 491, no. 7425 (2012): 574–577.

61. R. Esteban, A. G. Borisov, P. Nordlander, and J. Aizpurua, “Bridging Quantum and Classical Plasmonics with a Quantum Corrected Model,” *Nature Communications* 3 (2012): 825.

62. F. Benz, M. K. Schmidt, A. Dreismann, et al., “Single-Molecule Optomechanics in “Picocavities”,” *Science* 354, no. 6313 (2016): 726–729.

63. T. Giovannini, P. Grobas Illobre, P. Lafiosca, et al., “plasmonX: an Open-Source Code for Nanoplasmonics,” *Computer Physics Communications* 322 (2026): 110035, https://doi.org/10.1016/j.cpc.2026.110035.

64. L. Dong, X. Yang, C. Zhang, et al., “Nanogapped Au Antennas for Ultrasensitive Surface-Enhanced Infrared Absorption Spectroscopy,” *Nano Letters* 17, no. 9 (2017): 5768–5774.

65. J. Kozuch, K. Ataka, and J. Heberle, “Surface Enhanced Infrared Absorption Spectroscopy,” *Nature Reviews Methods Primers* 3, no. 1 (2023): 70.

66. J. Wang, Z. Xie, Y. Zhu, et al., “Surface-Enhanced Infrared Absorption Spectroscopy (SEIRAS) for Biochemical Analysis: Progress and Perspective,” *Trends in Environmental Analytical Chemistry* 41 (2024): e00226.

67. H. Ma, S.-Q. Pan, W.-L. Wang, et al., “Surface Enhanced Raman Spectroscopy: Current Understanding, Challenges, and Opportunities,” *ACS Nano* 18, no. 22 (2024): 14000–14019.

68. E. C. Le Ru and B. Auguié, “Enhancement Factors: A Central Concept during 50 Years of Surface-Enhanced Raman Spectroscopy,” *ACS Nano* 18, no. 14 (2024): 9773–9783.

69. T. Giovannini, S. Gómez, and C. Cappelli, “Modeling Raman Spectra in Complex Environments: From Solutions to Surface-Enhanced Raman Scattering,” *The Journal of Physical Chemistry Letters* 16, no. 12 (2025): 3106–3121.

70. F. D’Apuzzo, A. R. Piacenti, F. Giorgianni, et al., “Terahertz and Mid Infrared Plasmons in Three-Dimensional Nanoporous Graphene,” *Nature Communications* 8, no. 1 (2017): 14885.

71. W. Xu, N. Mao, and J. Zhang, “Graphene: A Platform for Surface-Enhanced Raman Spectroscopy,” *Small* 9, no. 8 (2013): 1206–1224.

72. X. Ling, L. Xie, Y. Fang, et al., “Can Graphene be used as a Substrate for Raman Enhancement?,” *Nano Letters* 10, no. 2 (2010): 553–561.

73. M. Barbry, P. Koval, F. Marchesin, et al., “Atomistic Near-Field Nanoplasmonics: Reaching Atomic-Scale Resolution in Nanooptics,” *Nano Letters* 15, no. 5 (2015): 3410–3419.

74. M. Urbieta, M. Barbry, Y. Zhang, et al., “Atomic-Scale Lightning Rod Effect in Plasmonic Picocavities: A Classical View to a Quantum Effect,” *ACS Nano* 12, no. 1 (2018): 585–595.

75. J. J. Baumberg, “Picocavities: A Primer,” *Nano Letters* 22, no. 14 (2022): 5859–5865.

76. G. Maccaferri, C. Zanardi, Z. Y. Xia, et al., “Systematic Study of the Correlation between Surface Chemistry, Conductivity and Electrocatalytic Properties of Graphene Oxide Nanosheets,” *Carbon* 120 (2017): 165–175.

77. Y. Miyajima, A. A. D. T. Adikaari, S. J. Henley, J. M. Shannon, and S. R. P. Silva, “Electrical Properties of Pulsed UV Laser Irradiated Amorphous Carbon,” *Applied Physics Letters* 92, no. 15 (2008): 152104.

Supporting Information

Additional supporting information can be found online in the Supporting Information section. **Supporting Fig. S1:** Schematic atomistic depiction of the different a-Carbon phases in their simulated unit cells. **Supporting Fig. S2:** ωFQ absorption spectra of the cured M34-2000 structure (generated from a 50% replication of the unit cell) using $\tau = 170$ a.u. and $\tau = 600$ a.u.. **Supporting Fig. S3:** ωFQ absorption spectra of the cured M34-2000 and M34-2500 structures (generated from a 50% replication of the unit cell), normalized by the total number of atoms. **Supporting Fig. S4:** ωFQ induced densities for *X*, *Y*, and *Z* field polarizations for M18-2000 (a,b) and M34-2000 (c,d) in their uncured (a,c) and cured (b,d) forms. The maps are provided within the central unit cell. **Supporting Fig. S5:** 2D field enhancement maps on *XY* planes for the uncured M18-2000 structure. **Supporting Fig. S6:** 2D field enhancement maps on *XZ* planes for the uncured M18-2000 structure. **Supporting Fig. S7:** 2D field enhancement maps on *YZ* planes for the uncured M18-2000 structure. **Supporting Fig. S8:** 2D field enhancement maps on *XY* planes for the cured M18-2000 structure. **Supporting Fig. S9:** 2D field enhancement maps on *XZ* planes for the cured M18-2000 structure. **Supporting Fig. S10:** 2D field enhancement maps on *YZ* planes for the cured M18-2000 structure. **Supporting Fig. S11:** 2D field enhancement maps on *XY* planes for the uncured M34-2000 structure. **Supporting Fig. S12:** 2D field enhancement maps on *XZ* planes for the uncured M34-2000 structure. **Supporting Fig. S13:** 2D field enhancement maps on *YZ* planes for the uncured M34-2000 structure. **Supporting Fig. S14:** 2D field enhancement maps on *XY* planes for the cured M34-2000 structure. **Supporting Fig. S15:** 2D field enhancement maps on *XZ* planes for the cured M34-2000 structure. **Supporting Fig. S16:** 2D field enhancement maps on *YZ* planes for the cured M34-2000 structure. **Supporting Table S1**: Structural descriptors for the M18 and M34 phases discussed in the paper, in both their as-prepared and cured forms. **Supporting Table S2:** Percent number of sites versus total number of carbon atoms that are available for saturation with a reactive water probe for the phases discussed in this paper, for both as-prepared and cured forms. **Supporting Table S3:** ωFQ parameters exploited in the calculations.[3] **Supporting Table S4:** Maximum electric field enhancement $|\mathbf{E}|/|\mathbf{E_0}|$ for the M34-2000 Cured structure (generated from a 50% replication of the unit cell) using $\tau = 170$ a.u. and $\tau = 600$ a.u. as a function of the field polarization. **Supporting Table S5:** Effective volume and effective area for M18-2000 and M34-2000a-C superstructures in their uncured and cured forms as a function of the field polarization calculated on the representative planes shown in Figure 3 in the main text.